Tuning the Drug Loading and Release of DNA-Assembled Gold-Nanorod Superstructures

*Vahid Raeesi, Leo Y. T. Chou, and Warren C. W. Chan**

Fundamental studies on the interactions of nanoparticles with biological systems in vitro and in vivo have presented new challenges in the chemical design of delivery vehicles for targeting cancer.[1] These studies have shown that particle sizes,[2–4] shapes,[5] and surface chemistry[6,7] may influence their interaction with serum proteins,[8] cells,[9,10] organs, tumors as well as how they are eliminated from the body. Recently, we have employed these fundamental findings in combination with DNA assembly[11–13] to develop a modular nanoparticle-delivery system that uses DNA to assemble nanoparticles into superstructures.[14] These delivery superstructures were based on a "core–satellite" architecture where a central "core" nanoparticle was uniformly decorated with "satellite" nanoparticles. The advantage of this system was not only the tunability in size, shape, and surface chemistry during synthesis but these nanosystems can be programmed to dynamically change its morphology to control the presentation of surface ligands and potentially navigate through different physico-chemical transport requirements in biological systems.[15] Additionally, these superstructures could be rationally designed to deliver medical agents to tumors and can disassemble in tumors to increase penetration depth or be renally cleared from the body. Using DNA to assemble inorganic nanoparticles allows for digital programmability (i.e., through sequence design) of the nanosystem structure. DNA also provides a natural capacity to associate with several anti-cancer therapeutics such as doxorubicin (Dox),[16] thus its design chemistry can affect absorption (loading) and desorption (release) of these drugs.[17–19] Finally, DNA hybridization/dehybridization follows thermodynamically predictable paths and its sensitivity to degradation can be engineered as a function of nanoparticle design.[20,21] As DNA-based delivery systems start to advance toward clinical use, there is a need to understand how combination of DNA and nanoparticles in a superstructure can be controlled to optimize therapeutic efficacy near cancer cells. Here, we build on our previous core–satellite design[14,15,22] study to show that loading and release of cancer therapeutics can be controlled by design. We showed that the DNA linker's chemistry affects the loading capacity and that we can modulate drug release rate using a photo-thermal core nanoparticle with specific DNA linker. We found an "additive" therapeutic effect on HeLa cancer cells by using a combination of heat and drug. This study shows the use of DNA and inorganic nanoparticle building blocks to engineer multifunctional delivery nanosystems with controllable therapeutic loading, release kinetics, and enhanced therapeutic effect.

Our core–satellite design consists of three main structural components: i) central core nanoparticles as structural scaffold, ii) DNA strands as molecular linkers, and iii) peripheral nanoparticles (satellite) as surface chemistry determinants. To utilize core–satellite assembly as a drug delivery carrier, we targeted DNA linker design to tune drug loading and its thermal denaturation to control drug release rate. To thermally denature DNA, we selected gold nanorods (GNRs) as the core nanoparticle because they have a high absorption cross section and photo-thermal conversion within the medical window (700–1000 nm).[23] The use of DNA to carry chemotherapeutic agents on the surface of gold nanorods have been previously demonstrated[24,25] but characterization of how DNA design can control loading and release was not fully examined. Additionally, the incorporation of satellite structures increase the total surface area per nanoparticle (Figure S1, Supporting Information) and enable layering within the nanosystem (different multiple drugs organized in different layers for sequential drug release). This provides greater flexibility in designing the nanosystems and the satellites can protect the DNA from exposed enzymatic cleavage.[14] In the future, the gold nanorods could be substituted with smaller heat-generating core structures such as CuS or silicon nanoparticles so all components could be eliminated (a key required to clinical translation of inorganic nanoparticles). We chose 5 nm spherical gold nanoparticles because our previous study showed they effectively protect the core particle from macrophage uptake when coated with a dense layer of the anti-fouling polymer poly-ethylene glycol.

Figure 1a illustrates the general process of engineering core–satellite drug carrier. We synthesized GNRs (28 nm × 7 nm)

Dr. V. Raeesi, Prof. W. C. W. Chan
Department of Material Science and Engineering
University of Toronto
Toronto, M5S 3E1, Canada
E-mail: warren.chan@utoronto.ca
Dr. V. Raeesi, Dr. L. Y. T. Chou, Prof. W. C. W. Chan
Institute of Biomaterials and Biomedical Engineering
University of Toronto
Toronto, Ontario M5S 3G9, Canada
Dr. L. Y. T. Chou
Dana-Farber Cancer Institute
Department of Cancer Biology
Harvard Medical School 44 Binney St., Boston, MA 02115, USA
Dr. L. Y. T. Chou
Wyss Institute for Biologically Inspired Engineering
Harvard University
3 Blackfan Circle, CLSB 5th Floor, Boston, MA 02115, USA
Prof. W. C. W. Chan
Department of Chemical Engineering
University of Toronto
Toronto, Ontario M5S 3E5, Canada
Prof. W. C. W. Chan
Department of Chemistry
University of Toronto
Toronto, Ontario M5S 3H6, Canada

DOI: 10.1002/adma.201600773

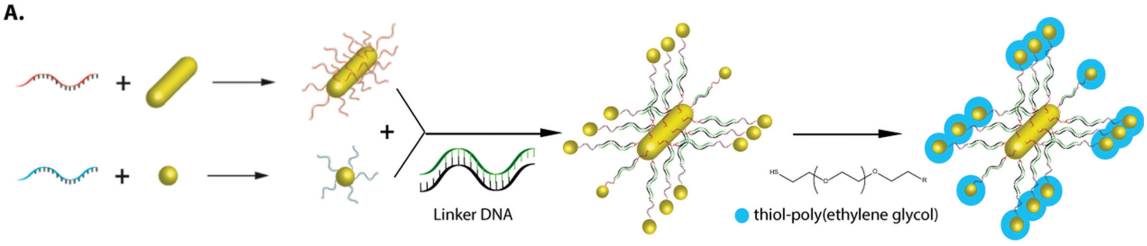

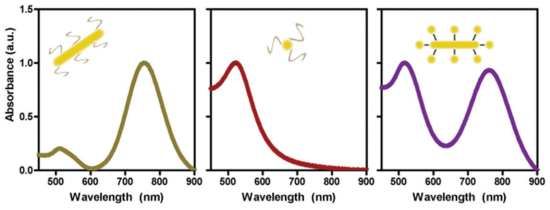

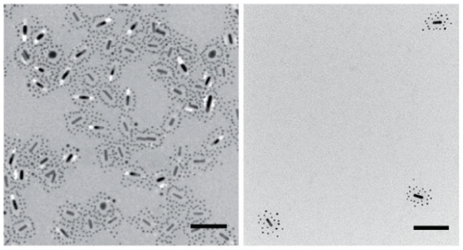

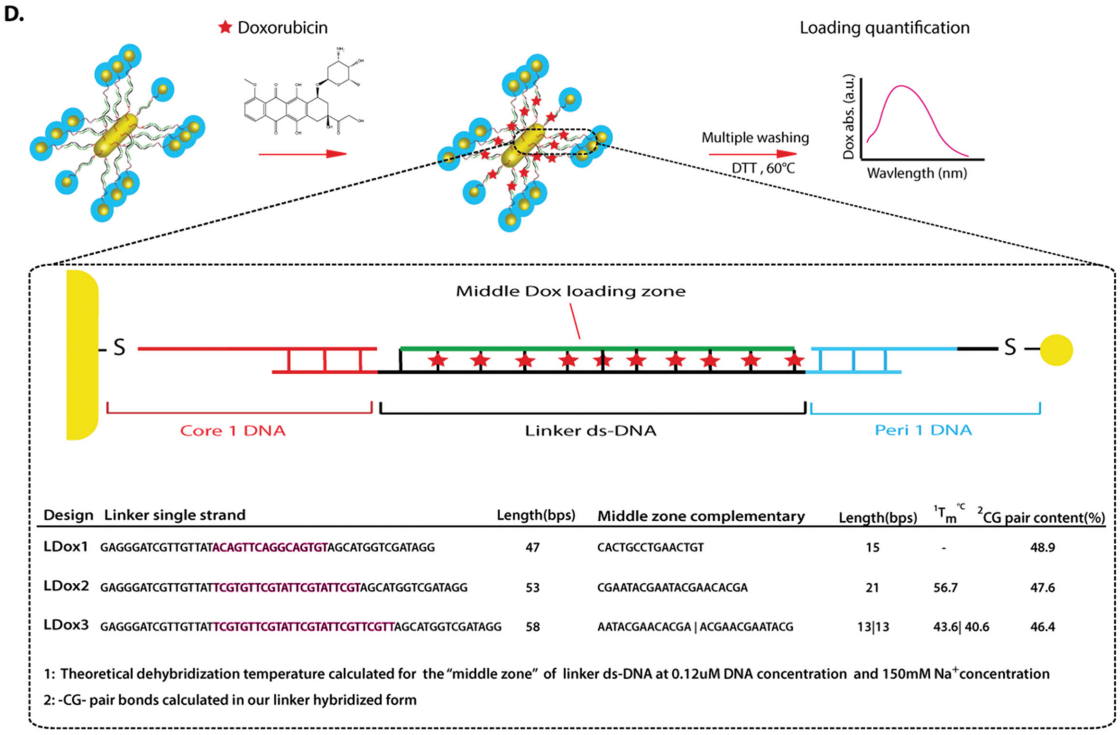

Design	Linker single strand	Length(bps)	Middle zone complementary	Length(bps)	$^{1}T_m$ °C	^{2}CG pair content(%)
LDox1	GAGGGATCGTTGTTATACAGTTCAGGCAGTGTAGCATGGTCGATAGG	47	CACTGCCTGAACTGT	15	-	48.9
LDox2	GAGGGATCGTTGTTATTCGTGTTCGTATTCGTATTCGTAGCATGGTCGATAGG	53	CGAATACGAATACGAACACGA	21	56.7	47.6
LDox3	GAGGGATCGTTGTTATTCGTGTTCGTATTCGTATTCGTTCGTTAGCATGGTCGATAGG	58	AATACGAACACGA | ACGAACGAATACG	13|13	43.6| 40.6	46.4

1: Theoretical dehybridization temperature calculated for the "middle zone" of linker ds-DNA at 0.12uM DNA concentration and 150mM Na^{+}concentration
2: -CG- pair bonds calculated in our linker hybridized form

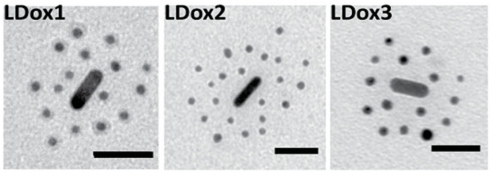

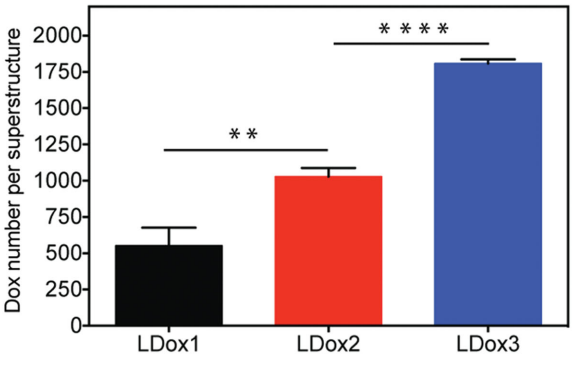

using a modified seed-mediated method.[26,27] A gold seed solution was first prepared using a directional cetyltrimethyl ammonium bromide (CTAB) surfactant followed by a growth process in excess gold cations and a moderate reducing agent, ascorbic acid. We then incubated the purified nanorods with thiolated core oligonucleotides (Core1 DNA) in tris-borate-EDTA (TBE) buffer to coat them with Core1 DNA (≈55 DNA per rod). Next, we prepared 5 nm gold nanoparticles as the satellites and coated them with satellite oligonucleotides (Peri1 DNA) at a valency of 2–3 DNA strands per particle.[14] This valency was sufficient to stabilizes the satellites during assembly process and low enough to leave the remaining surface satellites available for further ligand conjugation. To assemble the core–satellite superstructures, specific DNA linkers of variable length and sequence were used that connected these particles together through fixed complementary regions at their ends. We annealed a stoichiometric amount of DNA linkers (67 strand per core) with the core nanorods in a hybridization buffer which was maintained at 60 and 37 °C for 10 min and 1 h, respectively. After purification, linker–hybridized cores were hybridized with their corresponding linker's complementary strand to form double-stranded linkers. Next, we combined the linker–core with satellites under similar hybridization conditions at an excess molar ratio of 300 satellites per core to avoid possible assembly crosslinking. Following complete assembly, we back-filled the core–satellite superstructures with polyethylene glycol (PEG) to improve biological stability in serum-containing media and reduce non-specific interaction with biomolecules.[28] The core–satellite assembly was centrifugated and washed several times to remove excess PEG, oligonucleotides or gold nanoparticles. We first determined whether the assembly is successful by analyzing the distinct surface plasmons of core nanorods (740 nm) and satellite nanoparticles (517 nm) before and after assembly (Figure 1b). From normalized UV–vis spectrum, the assembly showed two dominant peaks at 740 and 520 nm. This suggested the presence of both nanorods and satellite particles in one assembly, resulting from the combination of nanorod's longitudinal plasmon at 740 nm and intense plasmon at 520 nm attributed to satellite particles. Figure 1c represents transmission electron microscopy (TEM) images of the assemblies.

We next explored the effect of core–satellite superstructure design on the loading capacity of therapeutic agents. We used the anticancer anthracycline drug Dox as the model therapeutic agent, which naturally intercalates into DNA. We investigated the effect of DNA linker design on Dox loading. We focused on the double-stranded region of the DNA linker as the main loading site relative to the short (15 base per strand) Core1 and Peri1 DNA attached directly to the particle. We formed core–satellite carriers using different linker duplex structures while keeping other components of the assembly constant. Figure 1d depicts the specifics of linker designs and doxorubicin loading process. Figure 1e provides TEM images of drug loaded core–satellite architectures. There are 22 ± 3 spherical satellite particles per GNR with an overall size of 70–90 nm for each superstructure. After optimizing the Dox loading process (Figure S2, Supporting Information), we chose to incubate each design with Dox feed concentration of 8 μg mL^{-1} for 5 h as this concentration showed loading value close to saturation point. After multiple washing, we directly disassembled the core–satellites using the reducing agent dithiothreitol at 60 °C for 1 h and collected the orange supernatant. We finally quantified the amount of Dox per carrier using absorbance measurements. In designing linkers, we considered three parameters: i) sequence length, ii) amount of −CG− base pairs for higher loading,[19] and iii) melting temperatures (T_m) of DNA linker duplex for Dox release. We varied the linker sequence length in three 47 bps (LDox1), 53 bps (LDox2), and 58 bps (LDox3) core–satellite designs and examined its effect on loading capacity. Each DNA linker contained 15 bases at both 5′ and 3′ ends that would hybridize with Core1 and Peri1 to form the assembly. We called the remaining middle sequence, the "middle loading zone." We designed the complementary sequences to the "middle loading zone" in LDox1, LDox2, and LDox3 to be 15, 21, and two 13 bps. We detected 552 ± 71, 1028 ± 35, and 1808 ± 17 Dox molecules per superstructure for LDox1, LDox2, and LDox3, respectively (Figure 1f). Figure S3 (Supporting Information) shows that there was minimum effect on the absorbance profile of the GNR-core superstructure after loading with doxorubicin. There is a linear increase in Dox loading capacity with increase in the size of the middle loading zone. Previous studies have allocated a minimum of three base pairs in DNA duplex for each Dox molecule.[29–31] When we calculated the number of base pairs per Dox molecule, we obtained a value less than three (Figure S4, Supporting Information). This suggests that the composition and architecture of the assembled system also

Figure 1. TDesign and drug loading characterization of GNR-core superstructures using DNA assembly. A) Individual gold nanorods (core) and spherical 5 nm nanoparticles (satellite) were coated with thiolated single-stranded DNA, which were then assembled together via linker DNA containing complementary sequence. Linker strands of different designs were used to tune Dox loading and release kinetics in the superstructure. Satellite particles located on the surface of these superstructures were then coated with PEG molecules, illustrated as blue clouds, to provide stability of superstructures in the buffer media. B) UV–vis absorption spectra of gold nanorods (left), spherical gold nanoparticles (middle), and their GNR core–satellite assembly (right). C) Transmission electron microscopy (TEM) images show formation of core–satellite shape architecture where spherical gold nanoparticles surround a single GNR in each individual superstructure. Scale bars are 100 nm. The TEM images show the core–satellite superstructure are interconnected but this is caused by drying of the sample on the grid. When we use a lower concentration, we see individual core–satellite nanoassembly (image to the right). D) Linker sequences of increasing length (47, 53, and 58 bps) with their specific complementary sequences were designed to change Dox loading capacity and melting temperature. Each linker was used to make a core–satellite superstructure, loaded with a constant Dox feed amount. The amount of loaded Dox was quantified by direct disassembly of the superstructure using dithiothreitol (DTT) and absorption measurements. E) Representative TEM images show formation of GNR core–satellite superstructures in all three linker designs. Scale bars are 30 nm. F) Effect of linker design (length) on Dox loading capacity per each superstructure. The increase in linker length from 47 to 58 bps, raised Dox loading capacity within the superstructure. (**$P < 0.005$ and ****$P < 0.0005$).

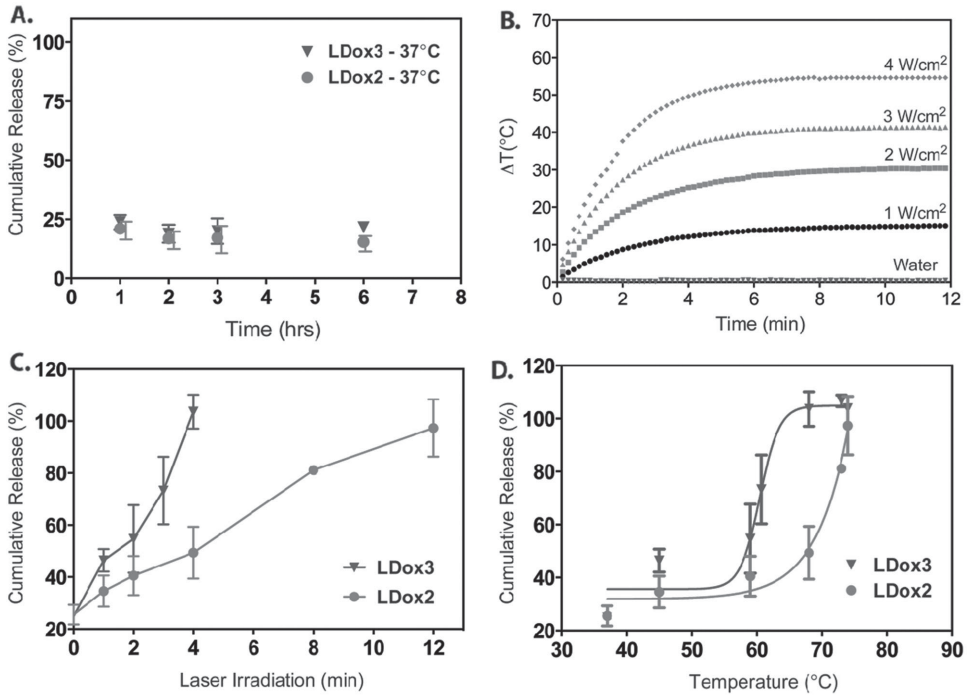

Figure 2. Normal and photo-thermal Dox-release characteristics in superstructures as a function of DNA linker design. A) Cumulative Dox release from LDox2 and LDox3 designs of superstructures at 37 °C in 6 h. B) Photo-thermal temperature elevation in colloidal superstructures as a function of laser power density. C) Cumulative photo-thermally triggered Dox release from LDox2 and LDox3 designs superstructures versus laser exposure time at 3 W cm^{-2}. D) Cumulative photo-thermally triggered Dox release from LDox2 and LDox3 designs superstructures versus photo-thermal temperature.

influence the loading capacity. The core–satellite superstructures also contain other DNA sequences (e.g., Core1 or Peri1), polyethylene glycol, and likely to contain residual amounts of positively charged CTAB[26,27] which may alter the availability of DNA sites for intercalation. Finally, the Core1 or Peri1 can also bind drugs but these sequences have a different purpose within the design of the superstructure. These sequences are designed to enable assembly but may not be ideal for intercalating drug molecules. We conclude that in engineering core–satellite superstructure carriers using DNA, increase in linker sequence length increase the loading capacity of Dox per core–satellite superstructure but the complex multi-component factors may interfere with predictive measures dictated by solo linker design.

We then explored the use of heat-generating core on Dox-release kinetics in LDox2 and LDox3 designs because these carriers showed the highest DOX loading. Drug-loaded DNA duplex can dehybridize when the local temperature is above melting temperature and release the Dox. Our design rationale for drug release was to use a linker sequence with a $T_m > 37$ °C so that the carrier shows minimum drug escape at physiological temperature but also low enough T_m that can provide rapid release using photo-thermal stimulation. Thus, we lowered the theoretical T_m of LDox3 by using two (13 bps) low T_m middle zone complementary sequences, 43.6 and 40.6 °C, compared to one 21 bps complementary sequence in LDox2 with $T_m \approx 56.7$ °C. We hypothesized that a decrease in a linker duplex's theoretical melting temperature can lead to faster Dox release from core–satellite carrier. We first examined whether the loaded Dox with core–satellite superstructures designed with LDox3 and LDox2 linkers can be released at physiological temperature (37 °C). Aliquots of each Dox carriers were incubated in PBS buffer at 37 °C, supernatants were sampled after centrifugation at different time points and the amount of Dox was quantified via spectrophotometry. Both designs demonstrated 25% non-specific release of Dox in the first hour (**Figure 2**a), but this remained constant afterward. This suggested a minor burst release at an initial stage followed by a plateau similar to common polymeric nanocarriers.[32,33] We attributed this to weakly bound Dox molecules on different components such as PEG-modified satellites of core–satellite structure that desorb at 37 °C. To control Dox release rate, we optically excited core–satellite superstructures by a near-infrared (IR) laser (785 nm) that closely matched GNR's longitudinal surface plasmon. This allowed us to increase the local temperature to be at or above the theoretical T_m of DNA linkers (Figure 2b and Figure S5, Supporting Information). Hence, DNA would melt leading to release of Dox and disassembly of core–satellite structure. After optimizations, our data (Figure S6 and S7, Supporting Information) confirmed the photo-thermal effect on controllable disassembly of core–satellite structure. The individual gold nanorods and nanoparticles remained structurally intact after excitation (no melting). We then measured Dox release under same laser exposure condition (Figure 2c). Complete release was triggered in 4 min for LDox3 versus 12 min for LDox2, about threefold increase in the average release rate. When release was plotted against the exposure temperatures (Figure 2d), we realized a similar release pattern to the DNA melting curves. We found the trigger Dox release in LDox3 to start at lower onset temperature ≈58 °C

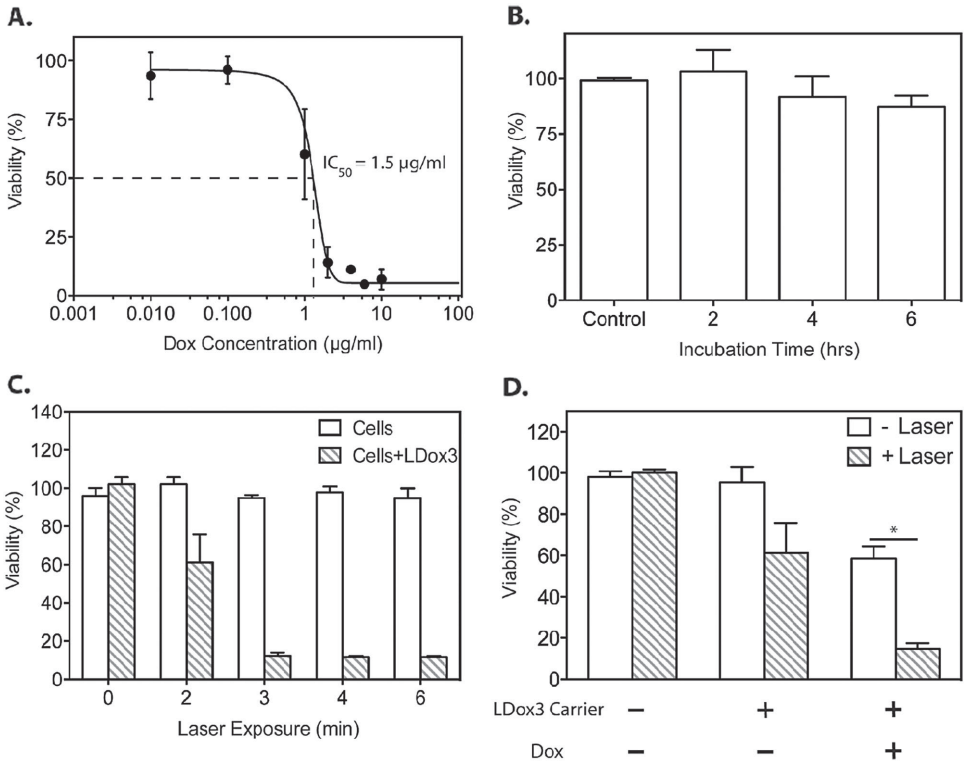

Figure 3. Cytotoxicity of Dox-loaded LDox3 superstructures on HeLa cancer cells. A) The inhibitory concentration of Dox at 50% viability (IC_{50}) of HeLa cells was calculated from fitted curve to be ≈1.5 μg mL^{-1}. This value is equivalent to almost half of the loaded Dox on to 3×10^{-9} M LDox3 superstructures. B) Toxicity test of superstructures (3×10^{-9} M) without Dox (unloaded) in 2, 4, and 6 h incubation with HeLa cells. The superstructures showed almost no toxicity in the absence of Dox. C) The effect of photo-thermal dose from unloaded superstructures (3×10^{-9} M) on HeLa cells. These titration data suggested 1–2 min photo-thermal dose (3 W cm^{-2}) for up to 40% cytotoxicity. D) Additive cytotoxicity (≈85%) of Dox-loaded superstructures (3×10^{-9} M) under optimized photo-thermal condition compared to ≈40% cytotoxicity of the same superstructures by either Dox or photo-thermal effect, individually. (*$P < 0.05$).

versus ≈68 °C for LDox2. Assigning an apparent release temperature (T_r) at 50% release of the fitted curves, we also calculated an ≈10 °C decrease from LDox2 (T_r = 71 °C) to LDox3 (T_r = 60 °C). Both analyses suggested lower temperature Dox release for LDox3 compared to LDox2. Our photo-thermal release data in GNR core–satellite exhibited similar behavior to previous reports on DNA-functionalized GNR carriers used for Dox release[25] or selective release of DNA.[33] We inferred that a decrease in the linker's melting temperature will lead to a lower required temperature for Dox release. This suggests that we can tune the drug release rate and temperature by changing the DNA linker sequence and composition.

We finally determined whether Dox-loaded superstructures can kill HeLa cancer cells. These experiments were designed to test whether the released drug is capable of killing the cells. The surface of the core–satellite nanosystem was not coated with cancer cell targeting agent because recent studies showed that there was no real difference between active and passive targeting for most nanoparticle sizes as large nanoparticles typically reside near the tumor vessel.[3,34,35] Thus, controlling the drug release process is quite important in future cancer nanomedicine applications, as large nanoparticles may not be able to easily penetrate the tumor to access the cells. Thus, future cancer nanomedicine therapy may focus strategies to alter the drug release profile, as small drug molecules can penetrate and kill tumor cells. We chose LDox3 design because it demonstrated highest Dox loading per carrier and rapid Dox release at lower laser-trigger temperature and dose. As Dox can kill cancer cells by intercalating their nuclear DNA, we first tested if the loaded Dox in core–satellites is still therapeutically active after release. Dox-loaded core–satellites were excited by laser and the released Dox was collected, and then was incubated with HeLa cells. The cytotoxicity was measured using a cell viability assay (tetrazolium salt XTT) compared to equivalent free molecular Dox control. The released Dox maintained its therapeutic activity (Figure S8, Supporting Information). We initially evaluated the effect of Dox and heat, individually, on HeLa cells, and then used these to test the effect of Dox-loaded core–satellites on cells with and without laser excitation. To learn the effect of Dox on HeLa cells, we measured viability of HeLa cells as a function of Dox concentration (**Figure 3**a). From fitted curve, we calculated the inhibitory concentration of Dox at 50% viability (IC_{50}) to be ≈1.5 μg mL^{-1}. We then tested the effect of unloaded core–satellites that is capable of loading twice IC_{50} Dox concentration with and without laser. HeLa cells were incubated with core–satellite superstructures for 2–6 h, washed, and then cell viability was measured. Core–satellites without drug and laser did not show toxicity on HeLa cells (Figure 3b). To determine the effect of heat on killing of cells, we incubated unloaded superstructures with HeLa cells and immediately

shun laser at 3 W cm^{-2} for 2–6 min. Incubation was continued for 3 h followed by viability measurement. HeLa cells were also excited with a laser in the absence of superstructures as a negative control. Figure 3c shows that laser radiation alone did not have any cytotoxic effect on the cells. In contrast, the presence of superstructures lead to ≈40% cytotoxicity following a 2 min (T = 60 °C) exposure to the laser. Further exposure to 3 min (T = 66 °C) increased the cytotoxicity to ≈90%. From 3 to 6 min exposure, there was no evident change in cytotoxicity. Finally, we explored the cytotoxicity of Dox-loaded superstructures on HeLa cells with and without laser (Figure 3d). Using the above data, we incubated 3×10^{-9} M of Dox-loaded superstructures for 2 h with HeLa cells and the viability was measured with and without laser. The laser treatment condition was 3 W cm^{-2} for 2 min. Without laser, Dox-loaded superstructures demonstrated ≈40% cytotoxicity which can be assigned to the non-specific 25% release of their loaded Dox (Figure S9, Supporting Information). Laser radiation on the same system induced 2.1-fold increase in cytotoxicity up to ≈85%. LDox3 superstructures release ≈50% of their Dox content after 2 min laser exposure which is equivalent to ≈1.5 μg mL^{-1}. As therapeutic activities of released Dox and molecular Dox are relatively the same, we inferred ≈50% cytotoxicity from released Dox on HeLa cells. Addition of Dox effect to ≈40% of heat cytotoxicity suggests an "additive" therapeutic effect (≈90%) core–satellite carriers on HeLa cells. We also ruled out non-thermal radiation effect of the laser on cytotoxicity of the Dox (Figure S10, Supporting Information). Regardless of laser-trigger, we conclude that Dox-loaded core–satellite carriers show therapeutic effect on HeLa cells but utilizing laser-trigger led to 2.1-fold increase in therapeutic effect as an additive effect of trigger-released Dox and photo-thermal heating.

We studied the design of the core–satellite superstructure as carriers of therapeutic agents. We demonstrated the design has a significant effect on the loading capacity and the loading capacity can be rationally controlled by sequence design. We were able to tune drug release rate by controlling linker thermal denaturation using photo-thermal stimulation. Using photo-thermally triggered rapid release and heat, we found 2.1-fold increase in therapeutic effect compared to no laser treatment. A next step will be to examine the therapeutic effect of these core–satellite structures in animal model. The current study presents a new strategy to control release of drugs from DNA–nanoparticle assembled superstructures and further promotes the use of assembly techniques to build delivery systems for biomedical applications. Building assemblies capable of dynamic change may be a key strategy to enable inorganic nanoparticles to navigate complex biological systems where different sizes, shapes, and surface chemistries for different biological systems may be needed to mediate their molecular interactions and transport patterns for effectively diagnosing and treating a disease.

Experimental Section

Materials: Chemical reagents related to nanorods and nanoparticles synthesis were purchased from Sigma–Aldrich. Methoxy-terminated poly(ethylene glycol) (mPEG–thiol, 5 kDa) was purchased from Laysan Bio. All oligonucleotides were purchased from Bio Basic and prepared as frozen stock solutions in ultrapure water (Nanopure) at –20 °C. Doxorubicin hydrochloride and Dulbecco's modified Eagle medium (DMEM) were purchased from Tocris and Gibco, respectively.

Synthesis and Characterization of "Core" Gold Nanorods: GNRs were grown via modified seed-mediated technique. Initially, seed solution was made by rapid injection of sodium borohydride (1.2 mL, 0.01 M) into a solution containing $HAuCl_4$ (0.5 mL, 0.01 M) and cetyltrimethyl ammonium bromide (19.5 mL, 0.1 M) under vigorous stirring. This solution was heated to 60 °C for 20 min under vigorous stirring followed by cooling to room temperature. Next, a growth solution of $HAuCl_4$ (49.5 mL, 0.01 M) and cetyltrimethyl ammonium bromide (950 mL, 0.1 M) was prepared. $AgNO_3$ (5 mL, 0.01 M) and ascorbic acid (7 mL, 0.1 M) were added subsequently to the above solution. The yellow color solution changed to clear. Then, 20 mL of the seed solution was added to the growth solution under moderate stirring and left overnight. The nanorods were centrifugated at 15 000 *g* for 30 min twice, washed with deionized (DI) water. The nanorods were characterized using transmission electron microscopy and UV–vis spectroscopy.

Synthesis and Characterization of "Satellite" Spherical Gold Nanoparticles: 5 nm gold nanoparticles were prepared via previously developed methods. $HAuCl_4$ (1 mL, 1% w/v) was added to 80 mL DI water and the solution heated to 60 °C on a stir plate. Reducing solution containing 4 mL trisodium citrate (1%), 1 mL tannic acid (1%), and 1 mL potassium carbonate (3.64 mg mL^{-1}) was prepared and heated to 60 °C for 50 min. While stirring, the reducing solution was rapidly injected into $HAuCl_4$ solution and the reaction was maintained at 60 and 90 °C for 30 and 10 min, respectively. The resulting nanoparticle solution was cooled down to room temperature followed by addition of 1 mL bis(*p*-sulfonatophenyl)phenylphospine dihydrate dipotassium salt (BSPP) and stirring overnight to improve stability. The particles were centrifugated (150 000 *g* for 35 min) and washed twice, re-dispersed in Tween 20 solution (0.01% w/v). The purified nanoparticles were characterized using transmission electron microscopy, dynamic light scattering, and UV–vis spectroscopy.

Oligonucleotide Functionalization of Core Gold Nanorods: The purified gold nanorods (20×10^{-9} M) was added to a mixture of thiolated Core1 oligonucleotide (10×10^{-6} M) and sodium dodecyl sulfate (0.2%). The mixture was incubated for 5 min followed by the addition of TBE buffer (2×, pH = 3, 1 M NaCl). The resulting solution was incubated over night at room temperature. The Core1 oligo-functionalized gold nanorods were purified by centrifugating twice at 12 000 *g* and washing.

Oligonucleotide Functionalization of Satellite Gold Nanoparticles: Gold nanoparticles (500×10^{-9} M) was added to a mixture of thiolated Peri1 oligonucleotide (5.7×10^{-6} M) and Tween 20 (0.1%). Next, 200 μL of trisodium citrate buffer (90×10^{-3} M, pH = 3) was added to the above mixture and aged for 30 min at room temperature. The Peri1 oligo-functionalized nanoparticles were purified by centrifugating twice at 150 000 *g* for 35 min and washing in phosphate buffered saline (1×, 0.01% Tween).

DNA Assembly of Core–Satellite Superstructures: Core1 oligo-functionalized gold nanorods (13.3×10^{-9} M) was added to a hybridization buffer containing LDox linker oligonucleotide (8×10^{-6} M), phosphate buffered saline (10×), $MgCl_2$ (50×10^{-3} M), and Tween 20 (0.01%) solutions. This solution was heat shocked at 60 °C for 10 min followed by incubation at 37 °C for 1 h. LDox-functionalized gold nanorods were cooled down to room temperature for 15 min, twice centrifugated at 15 000 *g* for 35 min at 4 °C and washed with phosphate buffered saline (1×, 0.01% Tween). The purified LDox-functionalized gold nanorods (5×10^{-9} M) was then hybridized with LDox middle-zone complementary strand (LDox-sp) in a buffer consisting LDox-sp (8×10^{-6} M), phosphate buffered saline (10×), $MgCl_2$ (50×10^{-3} M), and Tween 20 (0.01%) solutions at 37 °C for 1 h. Next, Peri1 oligo-functionalized satellite nanoparticles were added to the above solution and incubation was continued for 1 h at 37 °C. Finally, mPEG (10 mg mL^{-1}) was mixed with the above solution and maintained at 37 °C for another hour. The core–satellite assembly was purified using triple centrifugation at 12 000 *g* for 35 min at 4 °C and washing in phosphate buffered saline (1×, 0.01% Tween). The same procedure was applied for all three designs with the

same stoichiometry. In case of LDox3 design, only the hybridization step of complementary strand on to LDox-functionalized core nanorods was repeated consecutively due to two half complementary strands. Superstructures were characterized using transmission electron microscopy and UV–vis spectroscopy.

Quantification of Core–Satellite Superstructures Concentration: Each core–satellite superstructure consists of one GNR as the core particle that is surrounded with several spherical gold nanoparticles. Therefore, the number of superstructures in a solution would be equal to the number of their GNR core.

To measure GNR-core concentration in a superstructure solution, the peak intensity was measured at 740 nm from the absorption spectrum of superstructure solution, which is distinctly assigned to longitudinal surface plasmon (SPR) of GNRs (spherical gold nanoparticles SPR is at 520 nm and does not overlap with GNR's longitudinal SPR). This intensity was then correlated to GNR-core concentration using previously developed standard curves. The standard curves were prepared from a combination of data based on TEM (GNR dimensions), ICP (gold content in GNRs), and UV–vis absorption.

Loading and Quantification of Doxorubicin in the Core–Satellite Superstructures: Stock solution (1 mg mL^{-1}) of Dox in dimethyl sulfoxide (DMSO) was prepared, aliquoted and stored at −20 °C. Aliquots of Dox/DMSO (50 µL) were thawed at room temperature. Next, stoichiometric ratio of Dox/DMSO was incubated with colloidal solution of superstructures for 5 h at room temperature. The Dox-loaded superstructures were purified via triple centrifugation at 12 000 *g* for 30 min and washing in phosphate buffered saline (1×, 0.01% Tween).

To quantify the amount of loaded Dox per superstructure, relevant standard solutions of Dox were prepared and correlated to with their Dox absorption intensity at 480 nm peak. Next, known concentration of Dox-loaded superstructures (based on core nanorods) was incubated in dithiothreitol solution (1 M) at 60 °C for 1 h. The degraded particles were then centrifugated and the supernatant was collected. The amount of Dox in supernatant was calculated by absorption measurement at 480 nm and correlation to already developed standard curves. Experiments for individual batch of superstructures were conducted in triplicates.

Analysis of DNA Linker Base Pairs per Dox Molecule: In each GNR core–satellite superstructure, the total number of base pairs (potential sites for Dox loading) is calculated from the product of "total number of base pairs in each linker (M_1, Figure S3, Supporting Information)" by "the number of linkers per superstructure (N_1)." From the measured number of Core1 DNA (55 per superstructure) and average number of satellite nanoparticles per superstructure (22), N_1 becomes a value between maximum 55 ($N_{1,max}$) if all Core1 on GNR-core are linked to DNA linkers and minimum 22 ($N_{1,min}$). At least N_1 is equal to number of linkers that have connected the satellite nanoparticles to their GNR core in each superstructure. For a measured number of Dox per superstructure (N), the number of base pairs per Dox molecule (x) can be calculated from: $x = (N_1 \times M_1) / N$. In the analysis for each design, x was calculated for both boundary conditions of $N_{1,max}$ and $N_{1,min}$.

Photo-Thermal Setup and Experiments: The photo-thermal setup consists of a power adjustable fiber-coupled CW laser diode (785 nm) to excite superstructures and a high-resolution (320 × 240 pixels) thermal imager (FLIR E60) with ±2 °C thermal accuracy for monitoring the temperature. Photo-thermal experiments were performed in 96-well plates. In a general procedure, known concentration of superstructures in phosphate buffered saline (1×) solution (200 µL) was transferred into a well and was placed on a pre-heated stage (set to 37 °C). The sealed well-plate (to avoid evaporation) was stabilized for 10 min. Next, the laser drive was tuned to the desired power and a laser beam of 5 mm diameter was radiated on the well containing superstructures solution and the local average temperature raise of the well was registered with respect to a control well, as a function of time. The same process was applied to different concentrations and laser powers. Emissivity corrections were done using FLIR protocol with respect to black tape body (0.95).

Photo-Thermal Doxorubicin-Release Kinetic Experiments: Stock solutions of Dox-loaded superstructures with the specific linker were prepared and quantified for the amount of loaded Dox per superstructure. Next, aliquots of Dox-loaded superstructures (3×10^{-9} M) were prepared and maintained for 50 min at 37 °C before laser radiation. Each aliquot was assigned to a certain laser exposure time between 0 and 12 min. Similar to photo-thermal experiments, each aliquot was radiated by laser (3 W cm^{-2}) to its assigned exposure time and immediately ultracentrifugated at 150 000 *g* for 30 min at 4 °C. The supernatant was collected and quantified for the amount of released Dox by measuring absorption at 480 nm and relevant standard curves, similar to loading quantification process. This procedure was applied for both LDox2 and LDox3 designs in triplicates. Control release experiments were performed similarly without laser exposure at 37 °C for 1–6 h incubation time. Experiments for individual batch of superstructures were conducted in triplicates.

Cell Culture and Measurements of Dox Inhibitory Concentration at 50% Survival (IC_{50}): HeLa cancer cells (American Type Culture Collection) were maintained in DMEM supplemented with 10% fetal bovine serum (FBS) and 1% penicillin/streptomycin (P/S), at 37 °C and 5% CO_2 atmosphere. First, population doubling time (PDT) of this cell line was calculated from $PDT = t \times \ln(2)/\ln(X_e/X_b)$, where t is the incubation time, X_e is harvesting concentration, and X_b is seeding concentration. The PDT was measured to be ≈24.8 h.

To measure IC_{50} of free Dox molecules, 5000 HeLa cells were seeded in 96-well plate in triplicates and maintained in the incubator (37 °C, 5% CO_2) for one PDT. Next, old media was removed and different concentrations of Dox in DMEM (10% FBS, 1% P/S) were incubated with cells for 2.5 h. Dox/DMEM solution was removed and the cells were carefully washed once with pre-warmed (37 °C) phosphate buffered saline (1×). Fresh DMEM (10% FBS, 1% P/S) was again added to the cells and allowed incubation for another PDT. Old media was removed again and 100 µL phenol-free DMEM (10% FBS, 1% P/S) was added to each well followed by addition of XTT reagent. After 4 h incubation, absorption at 450 nm/650 nm (sample/reference) was measured using plate reader and cytotoxicity relative to control cells was calculated. Viability was plotted versus Dox concentration and IC_{50} value was derived from best curve fit.

Toxicity Measurements of Core–Satellite Superstructures: 5000 HeLa cells were seeded in 96-well plate in triplicates and maintained in the incubator (37 °C, 5% CO_2) for one PDT. Old media was removed and unloaded LDox3 design superstructures (3×10^{-9} M) in DMEM (10% FBS, 1% P/S) were incubated for 2, 4, and 6 h with the cells. The superstructure solutions were removed followed by cells washing and XTT procedure similar to cytotoxicity measurement for Dox molecules.

Cytotoxicity Measurements of Photo-Thermally Triggered Core–Satellite Superstructures: To measure the cytotoxic effect of solo generated heat by LDox3 superstructures, 5000 HeLa cells were seeded in 96-well plate in triplicates and maintained in the incubator (37 °C, 5% CO_2) for one PDT. Old media was removed and unloaded LDox3 superstructures (3×10^{-9} M) in DMEM (10% FBS, 1% P/S) were incubated with the cells for 15 min. The cells were then shun by laser (3 W cm^{-2}) for different exposure times (2–6 min) followed by incubation for another 2 h at 37 °C and 5% CO_2 atmosphere. Finally, the cells were washed once and XTT procedure was applied similar to previous cytotoxicity measurement sections. Control experiments with the same laser radiation doses were performed on the cells without superstructures.

The cytotoxic effect of Dox-loaded LDox3 superstructures was measured in a similar procedure. 5000 HeLa cells were seeded in 96-well plate in triplicates and maintained in the incubator (37 °C, 5% CO_2) for one PDT. Old media was removed and Dox-loaded LDox3 superstructures (3×10^{-9} M) DMEM (10% FBS, 1% P/S) were incubated with the cells for 15 min followed by laser (3 W cm^{-2}) radiation for 2 min. Incubation was continued for another 2 h. The cells were then washed once and XTT procedure was performed as previous sections. Control experiments with Dox-loaded superstructures on the cells without laser were done in parallel.

Supporting Information

Supporting Information is available from the Wiley Online Library or from the author.

Acknowledgements

The authors would like to acknowledge the Canadian Institute of Health Research (MOP-130143 and RMF-111623O), Natural Sciences and Engineering Research Council (NSERC, 2015-06397), and Prostate Cancer Foundation (D2014-12) for their financial support of the project. L.C. acknowledges the fellowship support from Canadian Breast Cancer Foundation and NSERC.

Received: February 8, 2016
Revised: April 21, 2016
Published online: August 9, 2016

[1] E. Blanco, H. Shen, M. Ferrari, *Nat. Biotechnol.* **2015**, *33*, 941.
[2] S. D. Perrault, C. Walkey, T. Jennings, H. C. Fischer, W. C. W. Chan, *Nano Lett.* **2009**, *9*, 1909.
[3] E. A. Sykes, J. Chen, G. Zheng, W. C. W. Chan, *ACS Nano* **2014**, *8*, 5696.
[4] E. C. Dreaden, L. A. Austin, M. A. Mackey, M. A. El-Sayed, *Ther. Delivery* **2012**, *3*, 457.
[5] L. Florez, C. Herrmann, J. M. Cramer, C. P. Hauser, K. Koynov, K. Landfester, D. Crespy, V. Mailänder, *Small* **2012**, *8*, 2222.
[6] J. V. Jokerst, T. Lobovkina, R. N. Zare, S. S. Gambhir, *Nanomedicine* **2011**, *6*, 715.
[7] Z. Yang, *Cancer Res.* **2004**, *64*, 6673.
[8] C. D. Walkey, J. B. Olsen, H. Guo, A. Emili, W. C. W. Chan, *J. Am. Chem. Soc.* **2012**, *134*, 2139.
[9] Q. Dai, C. Walkey, W. C. W. Chan, *Angew. Chem., Int. Ed.* **2014**, *53*, 5093.
[10] L. Shang, K. Nienhaus, G. U. Nienhaus, *J. Nanobiotechnol.* **2014**, *12*, 5.
[11] X. Xu, N. L. Rosi, Y. Wang, F. Huo, C. A. Mirkin, *J. Am. Chem. Soc.* **2006**, *128*, 9286.
[12] Y. Zhang, F. Lu, K. G. Yager, D. van der Lelie, *Nat. Nanotechnol.* **2013**, *8*, 865.
[13] Y. Chen, W. Cheng, *WIREs Nanomed. Nanobiotechnol.* **2012**, *4*, 587.
[14] L. Y. T. Chou, K. Zagorovsky, W. C. W. Chan, *Nat. Nanotechnol.* **2014**, *9*, 148.
[15] S. Ohta, D. Glancy, W. C. W. Chan, *Science* **2016**, *351*, 841.
[16] P. Mohan, N. Rapoport, *Mol. Pharmaceutics* **2010**, *7*, 1959.
[17] D. Agudelo, P. Bourassa, G. Bérubé, H.-A. Tajmir-Riahi, *Int. J. Biol. Macromol.* **2014**, *66*, 144.
[18] C. A. Frederick, L. D. Williams, G. Ughetto, *Biochemistry* **1990**, *29*, 2538.
[19] D. Kim, Y. Y. Jeong, S. Jon, *ACS Nano* **2010**, *4*, 3689.
[20] M. Reismann, J. C. Bretschneider, G. Plessen, U. Simon, *Small* **2008**, *4*, 607.
[21] R. Jin, G. Wu, Z. Li, C. A. Mirkin, G. C. Schatz, *J. Am. Chem. Soc.* **2003**, *125*, 1643.
[22] L. Y. T Chou, F. Song, W. C. W. Chan, *J. Am. Chem. Soc.* **2016**, *138*, 4565.
[23] Z. Qin, J. C. Bischof, *Chem. Soc. Rev.* **2012**, *41*, 1191.
[24] Z. Xiao, C. Ji, J. Shi, E. M. Pridgen, J. Frieder, J. Wu, O. C. Farokhzad, *Angew. Chem., Int. Ed.* **2012**, *51*, 11853.
[25] D. Wang, Z. Xu, H. Yu, X. Chen, B. Feng, Z. Cui, Bin Lin, Q. Yin, Z. Zhang, C. Chen, J. Wang, W. Zhang, Y. Li, *Biomaterials* **2014**, *35*, 8374.
[26] T. S. Hauck, T. L. Jennings, T. Yatsenko, J. C. Kumaradas, W. C. W. Chan, *Adv. Mater.* **2008**, *20*, 3832.
[27] N. R. Jana, *Small* **2005**, *1*, 875.
[28] K. Knop, R. Hoogenboom, D. Fischer, U. S. Schubert, *Angew. Chem., Int. Ed.* **2010**, *49*, 6288.
[29] J. B. Chaires, *Advances in DNA Sequence Specific Agents*, Elsevier Sciences, Cambridge, MA, USA, **1996**, p. 97.
[30] J. B. Chaires, K. R. Fox, J. E. Herrera, M. Britt, M. J. Waring, *Biochemistry* **1987**, *26*, 8227.
[31] J. B. Chaires, J. E. Herrera, M. J. Waring, *Biochemistry* **1990**, *29*, 6145.
[32] F. Tewes, E. Munnier, B. Antoon, L. N. Okassa, S. Cohen-Jonathan, H. Marchais, L. Douziech-Eyrolles, M. Soucé, P. Dubois, I. Chourpa, *Eur. J. Pharm. Biopharm.* **2007**, *66*, 488.
[33] H. S. Yoo, K. H. Lee, J. E. Oh, T. G. Park, *J. Controlled Release* **2000**, *68*, 419.
[34] A. Albanese, A. K. Lam, E. A. Sykes, J. V. Rocheleau, W. C. W. Chan, *Nat. Commun.* **2013**, *4*, 1.
[35] E. A. Sykes, Q. Dai, C. D. Sarsons, J. Chen, J. V. Rocheleau, D. M. Hwang, G. Zheng, D. T. Cramb, K. D. Rinker, W. C. W. Chan, *Proc. Natl. Acad. Sci. USA* **2016**, *113*, E1142.